



Published in final edited form as:

Med Phys. 2017 February ; 44(2): 558–569. doi:10.1002/mp.12048.

A supervoxel-based segmentation method for prostate MR images

Zhiqiang Tian,

Department of Radiology and Imaging Sciences, School of Medicine, Emory University, 1841 Clifton Road NE, Atlanta 30329, The United States

Lizhi Liu,

Department of Radiology and Imaging Sciences, School of Medicine, Emory University, 1841 Clifton Road NE, Atlanta 30329, The United States; Center for Medical Imaging and Image-guided Therapy, Sun Yat-Sen University Cancer Center, 651 Dongfeng East Road, Guangzhou 510060, P. R. China

Zhenfeng Zhang,

Center for Medical Imaging and Image-guided Therapy, Sun Yat-Sen University Cancer Center, 651 Dongfeng East Road, Guangzhou 510060, P. R. China

Jianru Xue, and

Institute of Artificial Intelligence and Robotics, Xi'an Jiaotong University, No.28 Xianning West Road, Xi'an 710049, P. R. China

Baowei Fei*

Department of Radiology and Imaging Sciences, School of Medicine, Emory University, 1841 Clifton Road NE, Atlanta 30329, The United States; Department of Biomedical Engineering, Emory University and Georgia Institute of Technology, 1841 Clifton Road NE, Atlanta 30329, The United States

Abstract

Purpose—Segmentation of the prostate on MR images has many applications in prostate cancer management. In this work, we propose a supervoxel based segmentation method for prostate MR images.

Methods—A supervoxel is a set of pixels that have similar intensities, locations, and textures in a 3D image volume. The prostate segmentation problem is considered as assigning a binary label to each supervoxel, which is either the prostate or background. A supervoxel-based energy function with data and smoothness terms is used to model the label. The data term estimates the likelihood of a supervoxel belonging to the prostate by using a supervoxel-based shape feature. The geometric relationship between two neighboring supervoxels is used to build the smoothness term. The 3D graph cut is used to minimize the energy function to get the labels of the supervoxels, which yields the prostate segmentation. A 3D active contour model is then used to get a smooth

* bfei@emory.edu; Baowei Fei., Website: <http://www.feilab.org/Home.html>.

The authors have no relevant conflicts of interest to disclose.

surface by using the output of the graph cut as an initialization. The performance of the proposed algorithm was evaluated on 30 in-house MR image data and PROMISE12 data set.

Results—The mean Dice similarity coefficients are $87.2 \pm 2.3\%$ and $88.2 \pm 2.8\%$ for our 30 in-house MR volumes and the PROMISE12 data set, respectively. The proposed segmentation method yields a satisfactory result for prostate MR images.

Conclusion—The proposed supervoxel based method can accurately segment prostate MR images and can have a variety of application in prostate cancer diagnosis and therapy.

Keywords

Segmentation; Prostate; Magnetic resonance image; Supervoxel

I. INTRODUCTION AND PURPOSE

Prostate cancer is the second leading cause of cancer mortality in American men¹. It was estimated that in 2016 there were 180,890 new cases of prostate cancer, and 26,120 deaths from prostate cancer in the United States¹. Magnetic resonance imaging (MRI) has become one of the most promising methods for prostate cancer diagnosis and MR images has also been used for targeted biopsy of the prostate. Segmentation of the prostate on MR images has many applications in the management of this disease^{2–4}. Registration between transrectal ultrasound (TRUS) and MRI can provide an overlay of MRI and TRUS images for targeted biopsy of the prostate^{5,6}.

There are extensive studies on prostate MR image segmentation^{3,7–16}. Among these methods, active contour model (ACM) based methods have been widely used due to their good performance^{11,17,18}. This method aims to evolve a curve, subject to constraints from a given image, in order to detect objects in that image. Kass¹⁹ proposed an active contour model that depends on the gradient of the image in order to stop the evolving curve on the boundary of the object. Chan and Vese¹⁷ proposed a level set formulation of the piecewise constant variant of the Mumford-Shah model²⁰ for image segmentation. Their model can detect an object whose boundary is not necessarily defined by image gradient. Tsai¹⁸ presented a shape-based method for curve evolution to segment medical images. A parametric model for an implicit representation of the curve is derived by applying the principal component analysis to a collection of signed distance representations of the training data. The parameters are then manipulated to minimize an objective function in order to get the segmentations. Qiu¹¹ proposed an improved ACM method incorporated into a rotational slice based 3D prostate segmentation to decrease the accumulated segmentation errors generated by the slice-by-slice method. A modified distance regularization level set algorithm was used to extract the prostate. Shape constraint and local region based energies were imposed to avoid the evolved curve to leak in regions with weak edges. Given a good initialization, ACM could yield a good segmentation result. However, it is a non-trivial task to get a good initialization. Therefore, ACM is difficult to get a global minimum of the energy function.

Another popular method for segmenting prostate segmentation is graph cut based algorithm. Graph cut (GC)^{21,22} is a global optimization tool, which gains more attentions due to its efficiency. Egger¹² proposed a graph-based approach to automatically segment the prostate central glands based on a spherical template. The rays travel through the surface points of a polyhedron to sample the graph nodes. The minimal cost on the graph was optimized by graph cut, which results in the segmentation of prostate boundaries and surface. Mahapatra and Buhmann¹³ proposed a fully automated method for prostate segmentation using random forests and graph cuts. The probability map of the prostate was generated by using image features and random forests classifier. The negative log-likelihood of the probability maps was considered as the penalty cost in a second-order Markov random field (MRF) cost function, which was optimized by graph cuts to get the final prostate segmentation. However, graph cut tends to leak at weak boundary. Fig. 1 shows the limitations of the graph cuts and the active contour model.

Combination of ACM and graph cut is a straightforward method to overcome the drawbacks of both methods. The graph cuts based active contour method^{23,24} has been proven effective for object segmentation in the computer vision field. They showed that the combination of graph cut and active contour can alleviate the disadvantages of both algorithms. Zhang et al.²⁵ proposed a graph cut based active contour model for kidney extraction in CT images. The experiments showed that the algorithm takes the advantages of graph cut and active contour for kidney CT segmentation. In our method, we combine graph cut and active contour in a cascade manner, which could yield better performance compared to an individual algorithm.

In this work, we propose a hybrid method, which combines graph cut and active contour model. This hybrid method takes the advantages from both GC and ACM, while it alleviates the effect from both disadvantages. The proposed prostate segmentation method is different from the aforementioned methods in the following aspects: 1) a 3D graph cuts and a 3D active contour model are combined in a cascade manner, which can yield accurate segmentation results. 2) The shape model is obtained based on each MR volume individually, which further improve the performance. This patient-specific shape model makes our method more robust across different prostate MR image data sets. 3) To the best of our knowledge, there is no report on 3D supervoxel based graph cuts segmentation for the prostate in MR images.

The remainder of the paper is organized as follows. In Section II, supervoxel-based prostate segmentation framework is introduced, which is followed by the details for each part of the proposed method. In Section III, we show the experimental results. We conclude this paper in Section IV.

II. METHOD

A. Framework of the proposed method

Fig. 2 shows the framework of the proposed method that consists of three parts: supervoxel generation, graph cuts, and 3D active contour model. The first part is the supervoxel generation, which is the basic processing unit in our method. After getting the supervoxels, a

neighborhood system is built by connecting supervoxel to each other. The second part is the supervoxel-based graph cuts. The supervoxel labeling problem is considered as a minimization of an energy function by using graph cuts. A supervoxel-based shape data term and a supervoxel-based smoothness term are computed to construct energy function. The segmentation result obtained by graph cuts tends to leak at the location with low image contrast. Therefore, a 3D active contour model is introduced to refine the segmentation obtained from graph cuts as the third part of the proposed method.

B. Supervoxel

In this work, we consider each point in an MR slice as a pixel instead of a voxel. A set of pixels, which have similar intensities, locations and textures in a slice, are called superpixel. Meanwhile, a set of pixels have similar intensities, locations and textures in an MR volume are considered as supervoxel, which represents a 3D tube.

Ideally, superpixels with similar intensities, locations and textures across image sequence should have same labels. However, most superpixel methods do not meet this requirement. To solve this problem, supervoxel is proposed to segment image slices into 3D tubes which can yield consistent image segmentation through the whole image volume. Xu and Corso²⁶ studied five supervoxel algorithms and measured the performance of these methods, which provides the details on the generation of supervoxels.

There are two advantages of using supervoxel for the proposed method. First, the supervoxel captures the local redundancy in the 3D medical image, which yields a small number of supervoxels. The small number of superpixels reduces the computational cost of the proposed algorithm significantly, e.g., for a 3D prostate MR image with a size of $320 \times 320 \times 100$, the number of voxels is over 10 million, while the number of supervoxels is only about 20,000 in our method. Second, a supervoxel containing more voxels makes the supervoxel-based feature more reliable, which can minimize the risk of assigning wrong labels to the supervoxels.

Fig. 3 shows the supervoxel and their geometric relationships. In this work, supervoxel is defined as follows.

$$SP_i = \{sp_i^j, j=1, \dots, |SP_i|\}, i=1, \dots, K \quad (1)$$

where K is the number of the supervoxels in an MRI volume. $|SP_i|$ is the number of slices contained in supervoxel i . sp_i^j is an intersection between supervoxel SP_i and slice j . In the MRI volume, different supervoxels may have different beginning slices and ending slices, which result in a different lifespan.

Since supervoxel is the basic processing unit of our method, it should satisfy two requirements. First, it should be efficient. Second, the number of supervoxels or the size of each supervoxel should be adjustable. Based on the requirements, simple linear iterative

clustering (SLIC)²⁷ algorithm is adopted to obtain the supervoxel. Fig. 4 shows an example of supervoxel map of an MR volume.

Instead of generating 2D regions and reconnecting in the third dimension, the supervoxels are directly generated in a 3D manner at one time. Here we give a brief introduction of the 3D supervoxel generation. First, k initial cluster centers are chosen on a 3D regular grid at the intervals of length $S = \sqrt{N/k}$ in all three dimensions. Second, the centers are moved to the lowest gradient position in a small local region. Third, the SLIC assigns each voxel to the new center based on spatial proximity and intensity. Then the algorithm iteratively computes the new centers and assigns the voxels. The iteration will stop after n iterations or until the distance between the new centers and previous one is small enough. Since SLIC does not guarantee that the supervoxel are fully connected, which means some isolated voxels are not assigned to any supervoxels. Therefore, a post-processing step enforces connectivity by re-assigning these voxels to nearby supervoxels.

C. Graph cut

For graph cuts, it seeks a labeling that minimizes the energy function as described below:

$$E(l) = E_{data}(l) + E_{smooth}(l) \quad (2)$$

The data term $E_{data}(l)$ evaluates the penalty for assigning a particular pixel to the object or background according to the prior knowledge; while the smoothness term $E_{smooth}(l)$ evaluates the penalty for assigning two neighboring pixels different labels in term of the given image data. In general, the data term is formulated as $E_{data}(l) = \sum_{i \in I} D_i(l_i)$, where D_i evaluates how well the label l_i fits the pixel i given the observed data. The choice of smoothness term is an important issue. Ideally, it should make labels smooth in the interior of the object and preserve discontinuity at the boundary of the object. Once the energy is defined, the graph cuts algorithm can be used to find a global minimum efficiently.

In our work, the prostate segmentation is considered as a labeling problem, where each supervoxel in the MR volume will be assigned a label $l_p, l_p \in \{1, 0\}$. Label 1 represents the prostate, while Label 0 corresponds to the background. The labels can be obtained by minimizing the energy function defined on an undirected graph $G = (V, E)$. V is a set of vertices correspond to supervoxels, and the edge E connects neighboring superpixels in a 3D neighborhood system, which will be introduced later. Our supervoxel-based energy function is formulated as follows:

$$E(l) = \sum_{p \in SP} D(l_p) + \gamma \cdot \sum_{\{p, q\} \in N} V(l_p, l_q) \quad (3)$$

where SP is a set of supervoxels, N represents the 3D neighborhood system, $\{p, q\}$ stands for two neighboring supervoxels in the 3D neighborhood system. The data term D quantifies the distance of each supervoxel to a proposed shape model. The smoothness term V

quantifies how likely two supervoxels have the same labels. The parameter γ balances the weight between the data term and the smoothness term. The graph cut method was implemented by using the public library “maxflow-v3.01”²⁸. The default weight parameter is fixed to $\gamma = 0.2$ in all of our experiments. Empirically, this weight is found to provide good results for all MR images.

1. Shape model based data term—To build the data term, a shape model is proposed to obtain the supervoxel-based shape feature. The basic idea is that the supervoxel is close to shape model will have a high probability to be labeled as the prostate. The shape model of the prostate is obtained based on user intervention, which could capture the shape variability more accurately for an individual prostate. While the automatic methods use population information to train a model to capture a statistical shape of the prostate on MR images. For segmenting the prostate on a new MR image, the patient-specific shape model plays more important role than statistical shape to guide the algorithm to segment the prostate. Therefore, the patient-specific shape model makes our method more robust across different data sets. In addition, it can obtain more consistent segmentation results than other automatic methods that are based on population information.

There are three steps to get the shape model. First, three key slices are selected from a 3D MR image, which are from the apex, base, and middle regions of the prostate. Second, four points are marked by the user for each of these three key slices. For each key slice, the four points are located at the boundary of the prostate. An initial prostate contour in one key slice can be determined through these four points. Therefore, 3 contours are obtained for the apex slice, based slice, and middle slice, respectively. Third, two semi-ellipsoids are fitted based on these 3 contours. One is toward to the apex slice based on the contours in the apex and middle slices, the other is toward to the base slice based on contours in the base and middle slices. Note that these two fitted surfaces of semi-ellipsoids are not accurate for the prostate, but it is good enough to be used for computing the shape feature.

Once the semi-ellipsoids are obtained, the prostate and background shape data terms can be defined as follows.

$$\begin{aligned} D(l_p=1) &= -\log p(SF_p|l_p=1) \\ D(l_p=0) &= -\log p(SF_p|l_p=0) \end{aligned} \quad (4)$$

where SF_p represents the mean value of shape feature of a supervoxel. $p(SF_p|l_p=1)$ and $p(SF_p|l_p=0)$ are calculated by using a distance transform based on the fitted semi-ellipsoids as follows.

$$p(SF_p|l_p=1) = 1 - p(SF_p|l_p=0) = \frac{1}{1 + \exp(-z)} \quad (5)$$

$$z = \kappa(d - \epsilon)$$

where d is the distance of a voxel to the surface of the fitted semi-ellipsoids, which computed by a fast implementation²⁹. κ controls the contrast between the inside and outside

of the shape model. ε controls the fatness of the shape model. In our experiments, the parameters κ and ε are set as 20 and 0.1 for all images, respectively.

The distance-based shape model is difficult to find the accurate boundaries between the prostate and the background by using voxels. Because the voxels on the both close sides of the prostate contour have a very similar distance to the fitted ellipsoids, it is difficult to separate these voxels based on the distance from the shape model. In contrast to voxels, supervoxels on the both close sides of prostate contour have distinguishing distance. Therefore, supervoxel is needed by shape model for segmenting prostate in our method.

In the proposed method, the shape feature is used to represent the supervoxels. Based on the feature of each supervoxel, the similarity of two neighboring supervoxels can be measured, which is smoothness term of the energy function in the GC method. In addition, the shape model can also describe the likelihood of each supervoxel belonging to the prostate or background, which is the data term of the energy function. Fig. 5 shows the supervoxel-based data term computed based on the shape model.

2. Smoothness term—The affinity of two neighboring supervoxels SP_p and SP_q are used to build the smoothness term. Therefore, the smoothness term is defined as follows.

$$V(l_p, l_q) = |l_p - l_q| \frac{|SP_p \cap SP_q|}{\max(|SP_p|, |SP_q|)} \quad (6)$$

where $|SP_p|$ and $|SP_q|$ are the number of slices of supervoxels SP_p and SP_q respectively. $SP_p \cap SP_q$ represents the number of common slices between two neighboring supervoxels. The smoothness term encourages that supervoxels have similar affinities and share more common slices to be labeled as same labels.

D. 3D Active contour model

The graph cut algorithm is an efficient method. However, the output of graph cut may be not satisfactory when the supervoxel algorithm cannot find the boundary of the prostate accurately. Because the supervoxel algorithm only uses local information in a small region to cluster voxels into a 3D supervoxel, it is hard to find the prostate boundary accurately, especially when the background has similar intensities and textures to that of the prostate. To solve this problem, the segmentation result obtained from the graph cut should be refined. In our method, 3D ACM is adopted to refine the prostate surface. Before presenting the 3D active contour model, a 2D active contour is reviewed first.

Let Ω denote the image domain, where $\Omega \subset R^N$. Considering an image I contains two regions, the object region to be segmented is denoted ω , the other is background region. The following model is proposed:

$$\min_{\omega, c_1, c_2} \int_{\omega} |I(x, y) - c_1|^2 dx dy + \int_{\Omega \setminus \omega} |I(x, y) - c_2|^2 dx dy + \mu |\partial \omega| \quad (7)$$

The last regularizing term ω represents the curve C weighted by a constant μ , and c_1 is the average value of I inside of ω , while c_2 is the average value of I outside of ω . Chan and Vese simplified the Mumford-Shah function as the following energy function:

$$\min_{\Phi, c_1, c_2} \left(\int_{\Omega} |I(x, y) - c_1|^2 H(\Phi(x, y)) dx dy + \int_{\Omega} |I(x, y) - c_2|^2 (1 - H(\Phi(x, y))) dx dy + \mu \int_{\Omega} |\nabla H(\Phi(x, y))| dx dy \right) \quad (8)$$

where H is the Heaviside function. Φ is a level set function, whose zero level set $C = \{x, y : \Phi(x, y) = 0\}$ segments the image into two regions, the object region $\{\Phi(x, y) > 0\}$ and the background region $\{\Phi(x, y) < 0\}$. The minimization of the energy is achieved by finding the level set function Φ and the constants c_1 and c_2 .

For 3D segmentation, the energy function is defined as follows:

$$\min_{\omega, c_1, c_2} \int_{\omega} |I(x, y, z) - c_1|^2 dx dy dz + \int_{\Omega \setminus \omega} |I(x, y, z) - c_2|^2 dx dy dz + \mu |\partial \omega| \quad (9)$$

Now, ω represents the surface S weighted by a constant μ . Following 2D simplification, the functional is simplified as the following energy function:

$$\min_{\Phi, c_1, c_2} \left(\int_{\Omega} |I(x, y, z) - c_1|^2 H(\Phi(x, y, z)) dx dy dz + \int_{\Omega} |I(x, y, z) - c_2|^2 (1 - H(\Phi(x, y, z))) dx dy dz + \mu \int_{\Omega} |\nabla H(\Phi(x, y, z))| dx dy dz \right) \quad (10)$$

Based on this model, the 3D active contour model could get smooth surface of the prostate, which can cover the shortage of the graph cut.

The work of Zhang et al.³⁰ was used in our method, which integrates edge and region-based segmentation in a simple equation as follows.

$$\Phi = \alpha(1 - \mu) + \beta \operatorname{div}(g \nabla \Phi) \quad (11)$$

Φ is a signed distance function, I is the image to be segmented, $g = g(|\nabla I|)$ is boundary feature map related to the image gradient. α and β are pre-defined parameters to balance these two terms. 3D ACM is implemented by using a 2D/3D image segmentation toolbox³¹. The parameters used in the toolbox are set as $\alpha = 1e - 6$ and $\beta = 1$ for all of our experiments.

Instead of dealing with the entire MR volume, ACM only considers an inner and outer region on both sides (15 voxels) from the fitted surfaces for detection of prostate. The number of iterations of 3D ACM is set as 5 in our experiment. If there is no change on the

surface between two iterations, the algorithm will stop early. The local evolution and small number of iterations guarantee that the ACM only smooths the segmented contour without changing the segmented contours in a major way.

E. Segmentation evaluation

The proposed method was evaluated based on four quantitative metrics, which are Dice similarity coefficient (DSC)^{32,33}, relative volume difference (RVD), Hausdorff distance (HD), and average surface distance (ASD)^{9,34}. The DSC is calculated as follows:

$$DSC = \frac{2|V_g \cap V_a|}{|V_g| + |V_a|} \quad (12)$$

where $|V_g|$ is the number of pixels of the prostate from the ground truth and $|V_a|$ is the number of pixels of the prostate from the segmentation of our method.

The relative volume difference is computed as follows:

$$RVD = 100 \times \left(\frac{|V_g|}{|V_a|} - 1 \right) \quad (13)$$

The RVD evaluates the algorithm whether tends to over-segment or under-segment the prostate. RVD is positive, if the algorithm under-segments the prostate and vice versa. To compute the HD and ASD, a distance from a pixel x to a surface Y is first defined as:

$$d(x, Y) = \min_{y \in Y} \|x - y\| \quad (14)$$

The HD between two surfaces X and Y is calculated by:

$$HD(X, Y) = \max\left\{\max_{x \in X} d(x, Y), \max_{y \in Y} d(y, X)\right\} \quad (15)$$

The ASD is defined as:

$$ASD(X, Y) = \frac{1}{|X| + |Y|} \left(\sum_{x \in X} d(x, Y) + \sum_{y \in Y} d(y, X) \right) \quad (16)$$

where $|X|$ and $|Y|$ represent the number of pixels in the surface X and Y , respectively.

III. EXPERIMENTAL RESULTS

A. Data

1. Our own data set—The proposed method was evaluated on our in-house prostate MR data set, which consists of 30 T2-weighted MR volumes. Transverse images were used in the experiments. The voxel sizes of the volumes are from 0.875 mm to 1 mm. The field of view varies from $200 \times 200 \text{ mm}^2$ to $333 \times 500 \text{ mm}^2$. No endorectal coil was used for our data acquisition. Each slice was manually segmented three times by two experienced radiologists. Majority voting is used to obtain the final ground truth from the six ground truths.

2. PROMISE12 data set—In addition, the PROMISE12 challenge data set³⁵ is used in our experiment, which has 50 training and 30 test MR images. The data set is transversal T2-weighted and from multi-center and multivendor. The MR images are acquired under different acquisition protocols, such as slice thickness and image size. The size of MR image is 512×512 (voxel size is $0.4 \times 0.4 \times 3.3 \text{ mm}^3$) or 320×320 (voxel size is $0.6 \times 0.6 \times 3.6 \text{ mm}^3$).

3. ISBI data set—The National Cancer Institute (NCI) Cancer Imaging Program in collaboration with the International Society for Biomedical Imaging (ISBI)³⁶ has launched a grand challenge involving 60 prostate MR images for training. The training dataset consists of axial scans with half obtained at 1.5 T with endo-rectal coil and other half at 3 T without endo-rectal coil. The T2-weighted MR sequences were acquired with 4 mm or 3 mm thickness, while the voxel size varies from 0.4 mm to 0.625 mm. The image size is from 320×320 to 400×400 .

B. Implementation details

The proposed method was implemented in MATLAB codes and C++ codes. The algorithm runs on an Ubuntu 14.04 desktop with an Intel Xeon CPU (3.4GHz) and 96 GB memory. Our code is not optimized and does not use parallel programming or multi-thread. The segmentation time is about 40 seconds for one 3D prostate MR image.

The user interaction time for manual segmentation varies between an experienced radiologist and a technician. The selection of the key slices and the initial points requires less than 30 seconds for a radiologist and about 1 minute for the trained technician.

C. Qualitative results

The qualitative results on our in-house MR images and the PROMISE12 MR images are shown in Fig. 6. Blue curves are ground truths from manually segmentations, while the red curves are the segmentations of the proposed method.

These images have different voxel sizes and image sizes, which shows the robustness of our method for different MR images. The qualitative results on our data set and PROMISE12 data set show that the supervoxel-based method is able to obtain satisfactory segmentation results.

D. Quantitative results

1. Our own data set—The quantitative evaluation results on our in-house 30 MR image volumes are shown in Table I. The values of four metrics, which are DSC, RVD, HD, and ASD, are posted in the table.

The proposed method yields a DSC of $87.19 \pm 2.34\%$, while it varies from 82.77% to 90.95%. It shows that the proposed method has a high accuracy and robustness. The mean RVD is negative, which shows that the proposed method tends to yield an over-segmented prostate. However, the value of mean RVD is -4.58% , which is very close to zero. This small RVD shows that the proposed method has a good balance between over-segmentation and under-segmentation. The value of HD measures the maximum distance between two surfaces, which is 9.92 ± 1.84 mm. The ASD is 2.07 ± 0.35 mm, which shows that the proposed method is able to segment the prostate with a relative small average surface distance.

2. PROMISE12 data set—Table II shows the segmentation results by the proposed method on PROMISE12 data set³⁵, which consists of 50 MR volumes. The proposed approach yielded a DSC of $88.15 \pm 2.80\%$, while the maximum is 92.92% and minimum is 81.80%. The RVD is $2.82 \pm 9.56\%$, while HD is 5.81 ± 2.01 mm, and ASD is 2.72 ± 0.77 mm. Details of the results are listed in Table II.

E. Comparison between supervoxel-based and voxel-based methods

To evaluate the advantage of using supervoxels compared with that of using voxels, we performed an experiment using our in-house data set. The DSC was used to evaluate the comparison results. In the experiment, both methods use the same framework of the proposed method. The DSC of the supervoxel-based method is $87.2 \pm 2.3\%$. For the voxel-based method, the DSC is $75.3 \pm 3.7\%$. Because the segmentation result of the voxel-based graph cut method is not good enough to be the initialization of ACM, the final result is worse than the supervoxel-based method.

F. Comparison with other methods and automatic version of the proposed method

The PROMISE12 data set is used for comparing our method with other prostate segmentation methods. Eight methods are used for the comparison, which are Imorphics³⁷, ScrAutoProstate³⁸, SBIA³⁹, grislies⁴⁰, Robarts⁴¹, ICProstateSeg⁴², V-net⁴³, and the automatic version of the proposed method.

The proposed method can be implemented in a fully automatic version. The straightforward way is that an automatic method is applied to substitute the user intervention to obtain the initialization for graph cuts. Milletari et al.⁴³ proposed a convolutional neural network based method for automatically segmenting the prostate on MR images. Therefore, the segmentation result of Milletari's method was selected as an initialization for the shape model of graph cuts in the proposed method. The implementation of this method is public available⁴⁴. We used the default parameters of Milletari's method.

Table III shows the comparison results in terms of DSC and HD. The results were shown as mean \pm standard deviation. DSC is available for all the methods, while HD are not available for all. Therefore, the hyphen is used in the table, which means that the corresponding measures are not reported in the papers. The proposed method gives the second higher DSC and the second lower standard deviation among all the methods. ScrAutoProstate³⁸ has the highest DSC of 90%, and very low standard deviation of 1.1%. For the HD, our method is at the second place. Although, ScrAutoProstate method has the highest DSC and Imorphics method has the lowest HD, our method has a relative good performances in terms of both DSC and HD at the same time.

G. Effect of the supervoxel size

Different supervoxel sizes have different performances. Bigger supervoxels contain more pixels to calculate features, which makes the supervoxel-based features more robust. But they may contain multiple classes, which may not be representative of one class. Smaller supervoxels contains less pixels, which are more homogeneous and the extracted features are representative of a single class. However, they may not always provide a sufficient number of voxels to calculate robust features.

For the SLIC method, the third dimension (z direction) of the 3D supervoxel must be same as the first dimension (x direction) and the second dimension (y direction) of the 3D supervoxel. This constraint leads to a poor quality of the 3D supervoxel. Therefore, the size of supervoxel on the xy-plane and z-plane is set separately, instead of using the same step size.

To evaluate the effect of supervoxel size on segmentation performance, our data set is used in this experiment. Fig. 7 shows the performance for different supervoxel sizes in terms of DSC(%) and HD(mm). This experiment shows that a good performance is achieved when the supervoxel size on the xy-plane is around 150.

H. The effect of the manual initialization

To evaluate the influence of the manual initialization, we performed two experiments using our in-house data set. The first experiment is evaluated the number of the points marked by the user on each key slice. The second experiment is to evaluate the effect of selecting three key slices, which are apex, base, and middle key slices. DSC is used as the metric to evaluate the influences.

For the first experiment, different numbers of the points marked by the user are chosen for performing the experiment. Fig. 8 is the evaluation result, which indicates that the proposed method is not sensitive to the number of points marked by the user.

For the second experiment, the user selects three key slices for the ellipsoid fitting. To individually evaluate the effect of selecting each key slice, two slices around each key slice are selected to run the algorithm, e.g., for evaluating the apex key slice Apex(i), two slices Apex(i-1) and Apex(i+1) are individually selected as the apex key slice to run the algorithm, where i presents the index of the slice. Fig. 9 shows the evaluation result, which indicates that the proposed method is not sensitive to the selection of the three key slices.

I. The effect of combining GC and ACM

To evaluate the performances of the supervoxel-based GC method and the ACM without supervoxel-based GC, we performed a segmentation experiment using PROMISE12 data set. Fig. 10 shows the performances of the supervoxel-based GC algorithm, ACM algorithm without supervoxel-based GC, and the proposed hybrid method. For the ACM algorithm without supervoxel-based graph cut, the semi-ellipsoids, which are fitted based on manual alignment, are used as the initialization. For the supervoxel-based GC method, the segmentation results are directly evaluated, which is not processed by the ACM algorithm.

Fig. 10 shows the average DSC of these two methods and our hybrid method. The DSC of the ACM without supervoxel-based GC is 72.35%, which is not satisfactory. This is because the initialization obtained without supervoxel-based GC is not good for ACM. For the supervoxel-based GC algorithm, the DSC is 81.67%, which is still not ideal. For the proposed hybrid method with both supervoxel-based GC and ACM, the performance is improved significantly, which is increased to 88.15%.

Fig. 11 shows the segmentation result of GC and the final segmentation result improved by using ACM.

J. The robustness comparison

To compare the robustness of our semi-automatic method with the automatic segmentation methods, a comparison experiment was performed. The implementations of most automatic methods in the PROMISE12 challenge are not available. Therefore, we chose a public available method called V-net^{43,44} for the robustness comparison, which is an automatic method with a comparable performance to our method and the top two methods of the PROMISE12 challenge on PROMISE12 data set.

Three data sets are used to compare the robustness of our semi-automatic method and the automatic V-net method. The data include our in-house data set with 43 MR images, the PROMISE12 data set with 50 MR images, and the ISBI data set with 60 MR images. The DSC is selected as the metric to evaluate the robustness. The segmentation results of two methods on three data sets are listed in Table IV.

The DSC of our semi-automatic method varies from 87.19 to 88.23 on three data sets, while the DSC of V-net is from 81.47 to 87.12. It shows that our method is more robust than the V-net method, which yields more consistent segmentation results. Our method has user intervention for initialization, could capture the shape variability more accurately across different data sets for an individual MR image. For segmenting prostate on a new MR image, our patient-specific shape model plays an important role to guide the algorithm to segment the prostate accurately.

IV. CONCLUSION

We proposed a supervoxel-based segmentation method for prostate MR images. The experiments on our own data set and public data set showed that the proposed method is able to accurately segment the prostate in MR volumes. Compared with a pixel-based method,

the proposed supervoxel-based algorithm significantly reduces the number of the computing points for MR volume segmentation. Meanwhile, the proposed method makes the graph cuts algorithm to be competent for handling big 3D medical data. The framework of the proposed method can be applied to segment other organs.

Experimental results on three different MR image data sets, including 30 in-house patient data, 50 RPOMISE12 data, and 60 ISBI MR Images, with different acquisition protocols from multiple centers and multiple vendors, showed that the proposed method can segment the prostate accurately in terms of four quantitative metrics. In addition, the proposed method generated low inter-observer variability introduced by manual initialization in term of DSC, which shows a high reproducibility. Another advantage of the proposed method is that it generated consistent segmentation result across three different data sets. This is important to deploy our method for image-guided biopsy in multiple centers. The experimental results of the proposed method shows that it has a potential to be used for image guided prostate interventions.

The automatic methods depend on the population information, which cannot cover all kinds of prostate shapes on MR images. Although, the public data set PROMISE12 collected from different centers with different protocols, the diversity of this data set is still not enough. We use patient-specific shape information obtained from user intervention, which could alleviate the drawback of these automatic methods. In addition, the models trained by the automated methods on a specific data set do not work well on the other new data sets that are not seen before. For a new data set, automated methods need to be trained on the new data set, which makes the deployment of these methods difficult. In contrast, our semi-automated method has a high reproducibility across different data sets, which is easy to be deployed in multiple centers.

The segmentation time of the ScrAutoProstate method is 1.1 second based on C++ implementation with parallelization. The computing time of the proposed method can be reduced by using C/C++ implementation of shape feature extraction and active contour instead of current MATLAB codes. Furthermore, parallel computing can be used on multiple CPU processors to accelerate the proposed method.

Acknowledgments

This research is supported in part by NIH grants R01CA156775 and R21CA176684, NSFC Project 61273252, Georgia Cancer Coalition Distinguished Clinicians and Scientists Award, and the Emory Molecular and Translational Imaging Center (NIH P50CA128301).

References

1. Siegel, Rebecca L., Miller, Kimberly D., Jemal, Ahmedin. Cancer statistics, 2016. CA: a cancer journal for clinicians. 2016; 66:7–30. [PubMed: 26742998]
2. Wu Y, Liu G, Huang M, Guo J, Jiang J, Yang W, Chen W, Feng Q. Prostate segmentation based on variant scale patch and local independent projection. IEEE transactions on medical imaging. 2014; 33:1290–1303. [PubMed: 24893258]
3. Litjens, Geert, Debats, Oscar, Barentsz, Jelle, Karssemeijer, Nico, Huisman, Henkjan. Computer-aided detection of prostate cancer in mri. IEEE transactions on medical imaging. 2014; 33:1083–1092. [PubMed: 24770913]

4. Akbari, Hamed, Fei, Bao Wei. 3D ultrasound image segmentation using wavelet support vector machines. *Medical physics*. 2012; 39:2972–2984. [PubMed: 22755682]
5. Hu, Yipeng, Ahmed, Hashim Uddin, Taylor, Zeike, Allen, Clare, Emberton, Mark, Hawkes, David, Barratt, Dean. Mr to ultrasound registration for image-guided prostate interventions. *Medical image analysis*. 2012; 16:687–703. [PubMed: 21216180]
6. Fei, Bao Wei, Nieh, Peter T., Schuster, David M., Master, Viraj A. PET-directed, 3D ultrasound-guided prostate biopsy. *Diagnostic imaging Europe*. 2013; 29:12–15. [PubMed: 25392702]
7. Qiu, Wu, Yuan, Jing, Ukwatta, Eranga, Sun, Yue, Rajchl, Martin, Fenster, Aaron. Fast globally optimal segmentation of 3d prostate mri with axial symmetry prior. *Medical image computing and computer-assisted intervention: MICCAI*. 2013; 16:198–205. [PubMed: 24579141]
8. Toth, Robert, Madabhushi, Anant. Multifeature landmark-free active appearance models: Application to prostate mri segmentation. *Medical Imaging, IEEE Transactions on*. 2012; 31:1638–1650.
9. Qiu W, Yuan J, Ukwatta E, Sun Y, Rajchl M, Fenster A. Prostate segmentation: An efficient convex optimization approach with axial symmetry using 3-d trus and mr images. *IEEE transactions on medical imaging*. 2014; 33:947–960. [PubMed: 24710163]
10. Gao, Yi, Sandhu, Romeil, Fichtinger, Gabor, Tannenbaum, Allen Robert. A coupled global registration and segmentation framework with application to magnetic resonance prostate imagery. *Medical Imaging, IEEE Transactions on*. 2010; 29:1781–1794.
11. Qiu, Wu, Yuan, Jing, Ukwatta, Eranga, Tessier, David, Fenster, Aaron. Three-dimensional prostate segmentation using level set with shape constraint based on rotational slices for 3d end-firing trus guided biopsy. *Medical physics*. 2013; 40:072903. [PubMed: 23822454]
12. Egger, Jan. Pcg-cut: graph driven segmentation of the prostate central gland. *PloS one*. 2013; 8:e76645. [PubMed: 24146901]
13. Mahapatra, Dwarikanath, Buhmann, Joachim M. Prostate mri segmentation using learned semantic knowledge and graph cuts. *Biomedical Engineering, IEEE Transactions on*. 2014; 61:756–764.
14. Tian, Zhiqiang, Liu, Lizhi, Fei, Bao Wei. *Proc SPIE Medical Imaging*. 2015. A supervoxel-based segmentation for prostate mr images.
15. Tian, Zhiqiang, Liu, Lizhi, Zhang, Zhenfeng, Fei, BaoWei. Superpixel-based segmentation for 3d prostate mr images. *Medical Imaging, IEEE Transactions on*. 2016; 35:791–801.
16. Tian, Zhiqiang, Liu, Lizhi, Fei, Bao Wei. *Proc SPIE Medical Imaging. SPIE*; 2015. A fully automatic multi-atlas based segmentation method for prostate mr images.
17. Chan, Tony F., Vese, Luminita A. Active contours without edges. *Image processing, IEEE transactions on*. 2001; 10:266–277.
18. Tsai, Andy, Yezzi, Anthony, Jr, Wells, William, Tempany, Clare, Tucker, Dewey, Fan, Ayres, Grimson, W Eric, Willsky, Alan. A shape-based approach to the segmentation of medical imagery using level sets. *Medical Imaging, IEEE Transactions on*. 2003; 22:137–154.
19. Kass, Michael, Witkin, Andrew, Terzopoulos, Demetri. Snakes: Active contour models. *International journal of computer vision*. 1988; 1:321–331.
20. Mumford, David, Shah, Jayant. Optimal approximations by piecewise smooth functions and associated variational problems. *Communications on pure and applied mathematics*. 1989; 42:577–685.
21. Boykov, Yuri, Veksler, Olga, Zabih, Ramin. Fast approximate energy minimization via graph cuts. *Pattern Analysis and Machine Intelligence, IEEE Transactions on*. 2001; 23:1222–1239.
22. Boykov, Yuri Y., Jolly, M-P. Interactive graph cuts for optimal boundary & region segmentation of objects in nd images. *Computer Vision, 2001. ICCV 2001. Proceedings. Eighth IEEE International Conference on; IEEE*; 2001. p. 105–112.
23. Xu, Ning, Ahuja, Narendra, Bansal, Ravi. Object segmentation using graph cuts based active contours. *Computer Vision and Image Understanding*. 2007; 107:210–224.
24. Kim, Jong-Sung, Hong, Ki-Sang. A new graph cut-based multiple active contour algorithm without initial contours and seed points. *Machine Vision and Applications*. 2008; 19:181–193.
25. Zhang, Pin, Liang, Yanmei, Chang, Shengjiang, Fan, Hailun. Kidney segmentation in ct sequences using graph cuts based active contours model and contextual continuity. *Medical physics*. 2013; 40:081905. [PubMed: 23927319]

26. Chenliang, Xu, Corso, Jason J. IEEE Conference on Computer Vision and Pattern Recognition (CVPR). 2012. Evaluation of Super-Voxel Methods for Early Video Processing; p. 1202-1209.
27. Achanta, Radhakrishna, Shaji, Appu, Smith, Kevin, Lucchi, Aurelien, Fua, Pascal, Susstrunk, Sabine. Slic superpixels compared to state-of-the-art superpixel methods. Pattern Analysis and Machine Intelligence, IEEE Transactions on. 2012; 34:2274–2282.
28. <http://vision.csd.uwo.ca/code/>.
29. Felzenszwalb, Pedro F., Huttenlocher, Daniel P. Distance transforms of sampled functions. Theory of computing. 2012; 8:415–428.
30. Zhang, Yan, Matuszewski, Bogdan J., Shark, Lik-Kwan, Moore, Christopher J. Medical image segmentation using new hybrid level-set method. Fifth International Conference BioMedical Visualization; IEEE; 2008. p. 71-76.
31. <https://www.mathworks.com/matlabcentral/profile/authors/1930065-yan-zhang>.
32. Fei, Bao Wei, Yang, Xiaofeng, Nye, Jonathon A., Aarsvold, John N., Raghunath, Nivedita, Cervo, Morgan, Stark, Rebecca, Meltzer, Carolyn C., Votaw, John R. Mr/pet quantification tools: Registration, segmentation, classification, and mr-based attenuation correction. Medical physics. 2012; 39:6443–6454. [PubMed: 23039679]
33. Yang, Xiaofeng, Wu, Shengyong, Sechopoulos, Ioannis, Fei, Baowei. Cupping artifact correction and automated classification for high-resolution dedicated breast ct images. Medical physics. 2012; 39:6397–6406. [PubMed: 23039675]
34. Garnier, Carole, Bellanger, J-J., Wu, Ke, Shu, Huazhong, Costet, Nathalie, Mathieu, Romain, De Crevoisier, Renaud, Coatrieux, J-L. Prostate segmentation in hifu therapy. Medical Imaging, IEEE Transactions on. 2011; 30:792–803.
35. Litjens, Geert, Toth, Robert, van de Ven, Wendy, Hoeks, Caroline, Kerkstra, Sjoerd, van Ginneken, Bram, Vincent, Graham, Guillard, Gwenael, Birbeck, Neil, Zhang, Jindang, et al. Evaluation of prostate segmentation algorithms for mri: the promise12 challenge. Medical image analysis. 2014; 18:359–373. [PubMed: 24418598]
36. Nicholas, Bloch, Anant, Madabhushi, Henkjan, Huisman, John, Freymann, Justin, Kirby, Michael, Grauer, Andinet, Enquobahrie, Carl, Jaffe, Larry, Clarke, Keyvan, Farahani. Nci-isbi 2013 challenge: Automated segmentation of prostate structures. 2015. <http://doi.org/10.7937/K9/TCIA.2015.zF0vIOPv>
37. Vincent, Gwenael Guillard Graham, Bowes, Mike. MICCAI Grand Challenge: Prostate MR Image Segmentation. 2012. Fully automatic segmentation of the prostate using active appearance models.
38. Birkbeck, Neil, Zhang, Jingdan, Requardt, Martin, Kiefer, Berthold, Gall, Peter, Zhou, S Kevin. MICCAI Grand Challenge: Prostate MR Image Segmentation. 2012. Region-specific hierarchical segmentation of mr prostate using discriminative learning.
39. Ou, Guray Erus Yangming, Doshi, Jimit, Davatzikos, Christos. MICCAI Grand Challenge: Prostate MR Image Segmentation. 2012. Multi-atlas segmentation of the prostate: A zooming process with robust registration and atlas selection.
40. Kirschner, Florian Jung Matthias, Wesarg, Stefan. MICCAI Grand Challenge: Prostate MR Image Segmentation. 2012. Automatic prostate segmentation in mr images with a probabilistic active shape model.
41. Yuan, Jing, Qiu, Wu, Ukwatta, Eranga, Rajchl, Martin, Sun, Yue, Fenster, Aaron. An efficient convex optimization approach to 3d prostate mri segmentation with generic star shape prior. MICCAI Grand Challenge: Prostate MR Image Segmentation. 2012
42. Gao, Daniel Rueckert Qinquan, Edwards, Philip. MICCAI Grand Challenge: Prostate MR Image Segmentation. 2012. An automatic multi-atlas based prostate segmentation using local appearance-specific atlases and patch-based voxel weighting.
43. Milletari, Fausto, Navab, Nassir, Ahmadi, Seyed-Ahmad. arXiv preprint arXiv: 1606.04797. 2016. V-net: Fully convolutional neural networks for volumetric medical image segmentation.
44. <https://github.com/faustomilletari/VNet>.

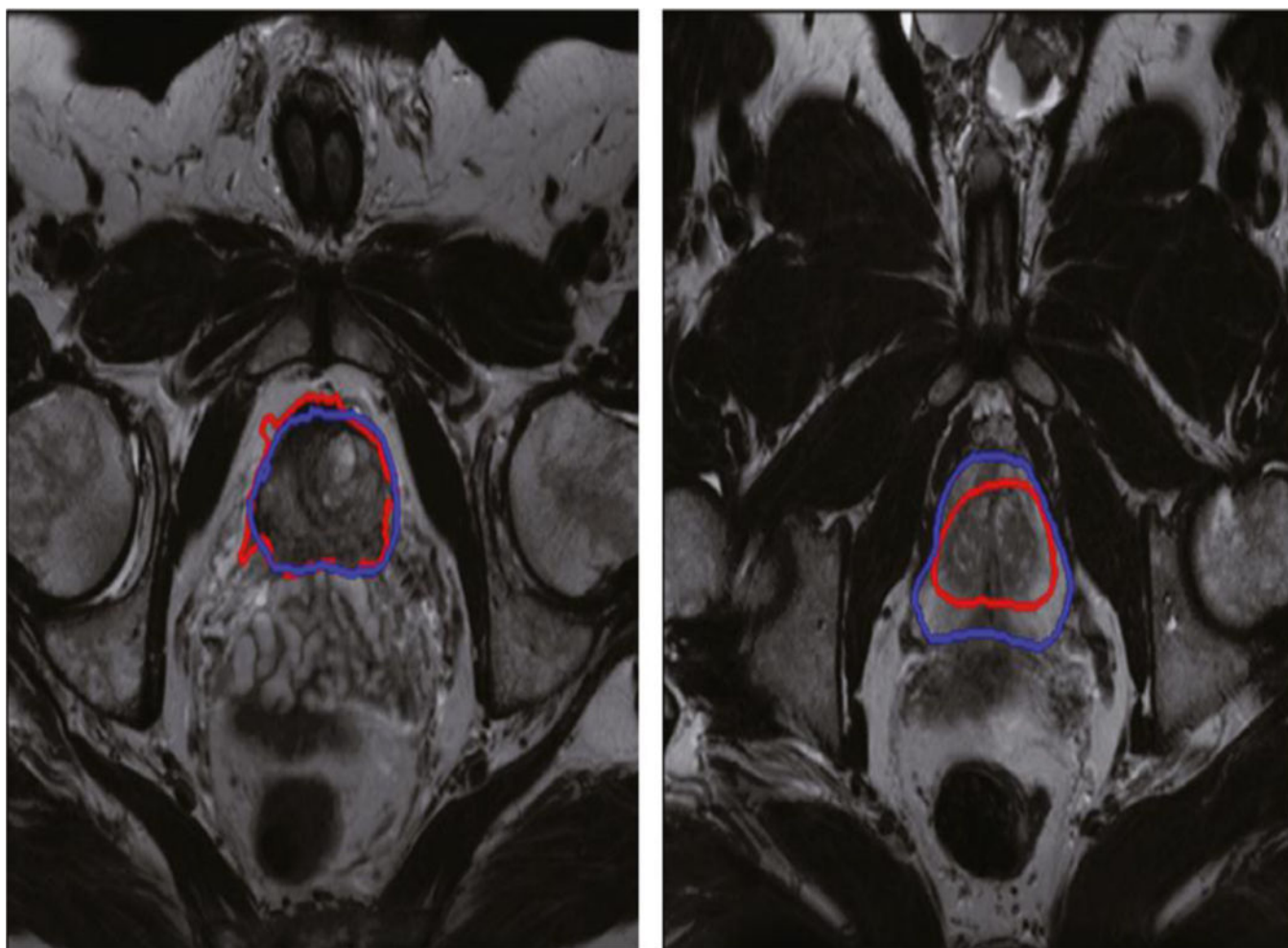


FIG. 1. Limitations of the graph cut method and the active contour model based method for prostate segmentation. Blue curve is the ground truth from manual segmentation by a radiologist, while the red curves are the segmented contours by the computer algorithms. Left figure is the segmentation result obtained by graph cuts, while the right figure is the segmentation result obtained by active contour model. The graph cut method tends to leak at the location with low image contrast, while the active contour model based method may fall at local minima based on an inaccurate initialization.

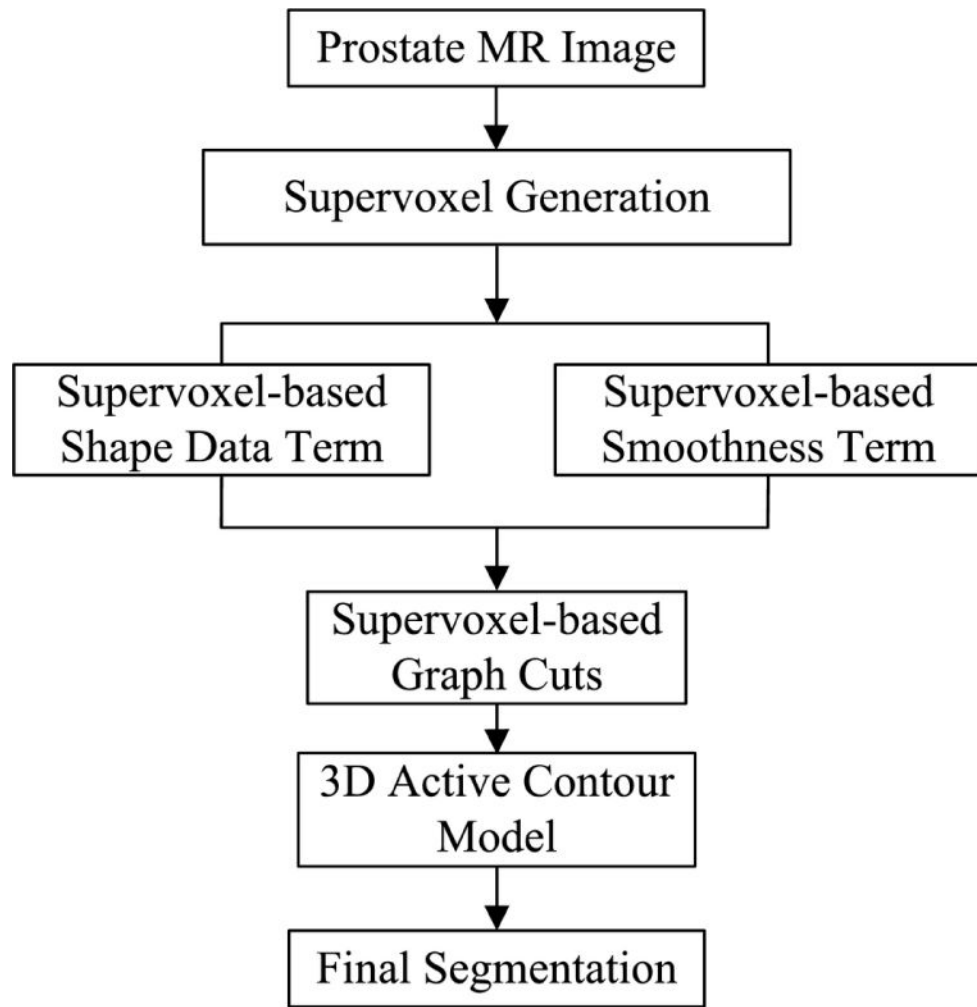


FIG. 2.
The framework of the proposed method.

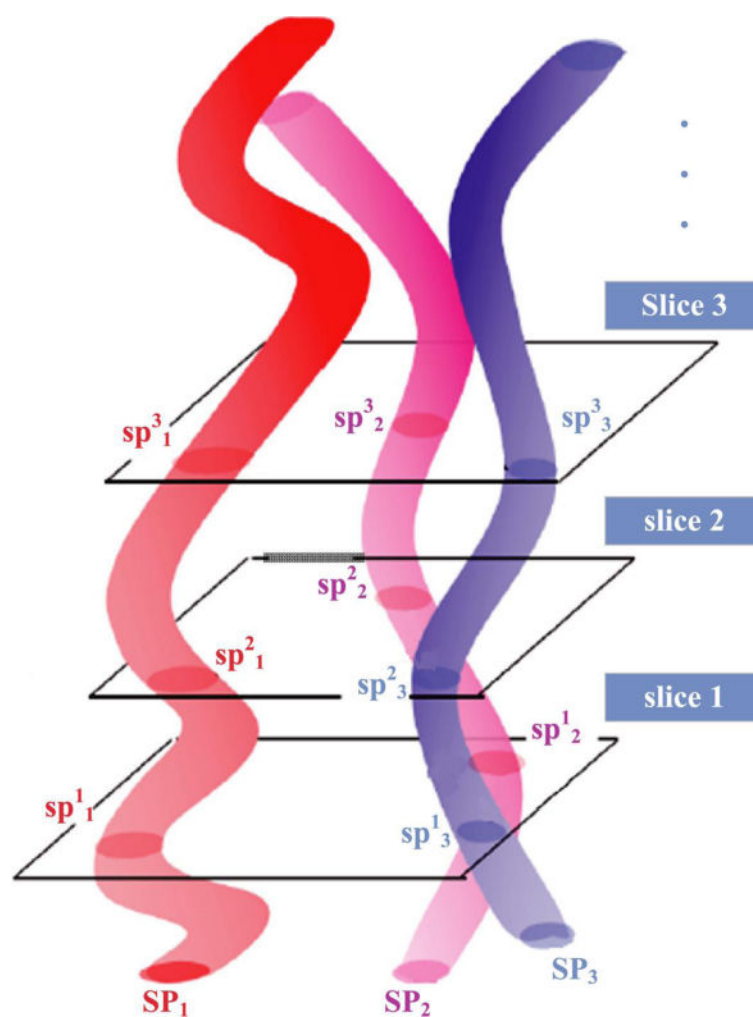
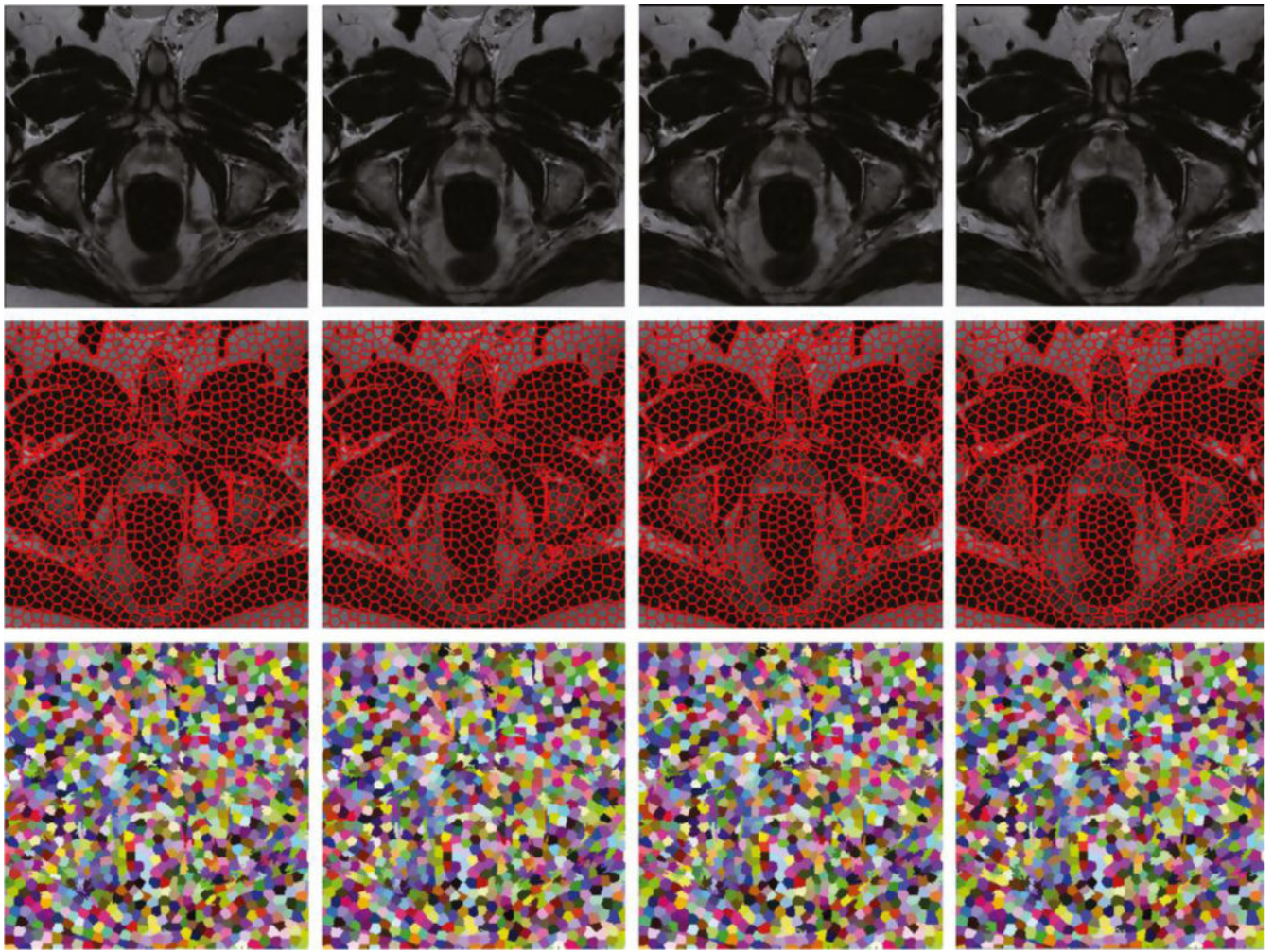
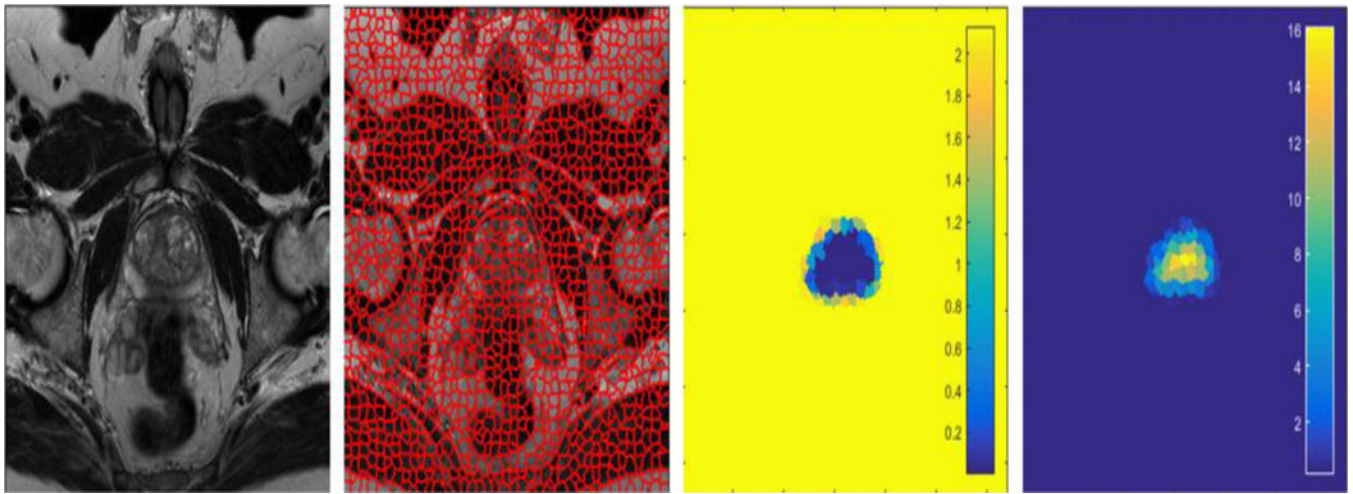


FIG. 3. Supervoxels and their geometric relationships. Different colored 3D tubes represent three supervoxels in the slice sequence.

**FIG. 4.**

Top: Four consecutive slices from a typical MR volume. Middle: The corresponding supervoxel maps. The red color is the boundaries of supervoxels. Bottom: The colored supervoxel maps, while same color through four slices means the same supervoxel.

**FIG. 5.**

The supervoxel-based data term. The first image is one original image slice of the prostate MR. The second image is the corresponding supervoxel map. The third image is the foreground shape data term. If the supervoxels are assigned as the foreground, the penalties of the shape model are shown in color. Blue color represents a low penalty, while yellow color represents a high penalty. The fourth image is the background shape data term. The color has same meaning with the foreground shape data term.

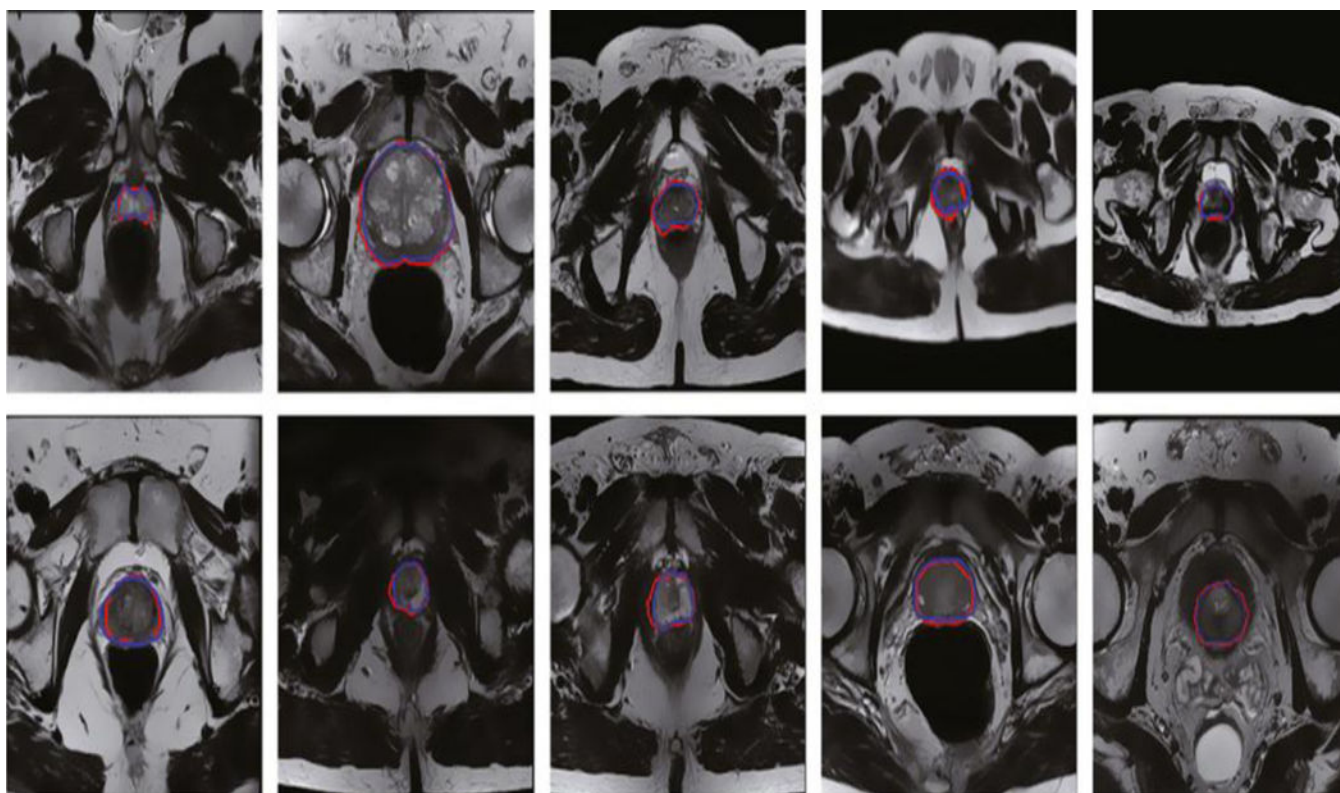


FIG. 6.
The qualitative results on two data sets. Top: Segmentation results on our in-house MR images. Bottom: Segmentation results on the PROMISE12 MR images.

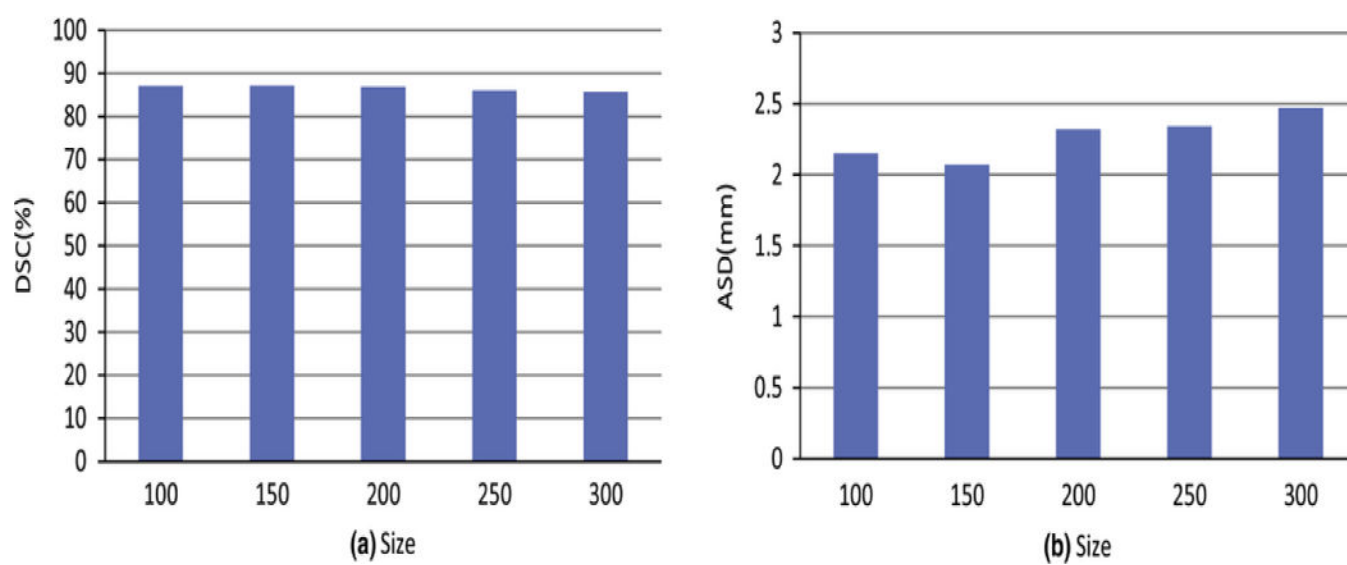


FIG. 7.
The effect of the supervoxel size on the xy-plane.

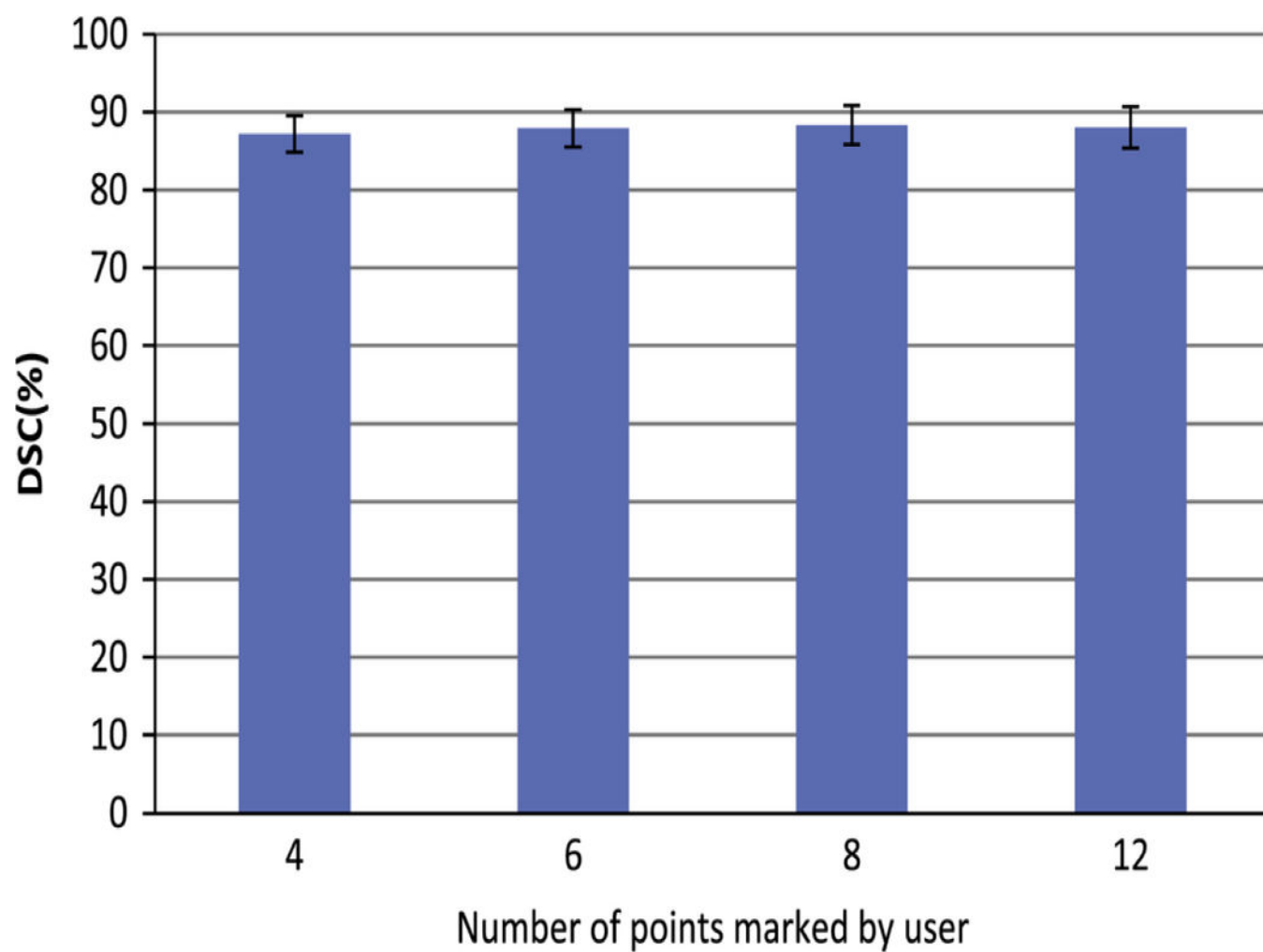


FIG. 8.
The effect of the number of initial points on segmentation performance.

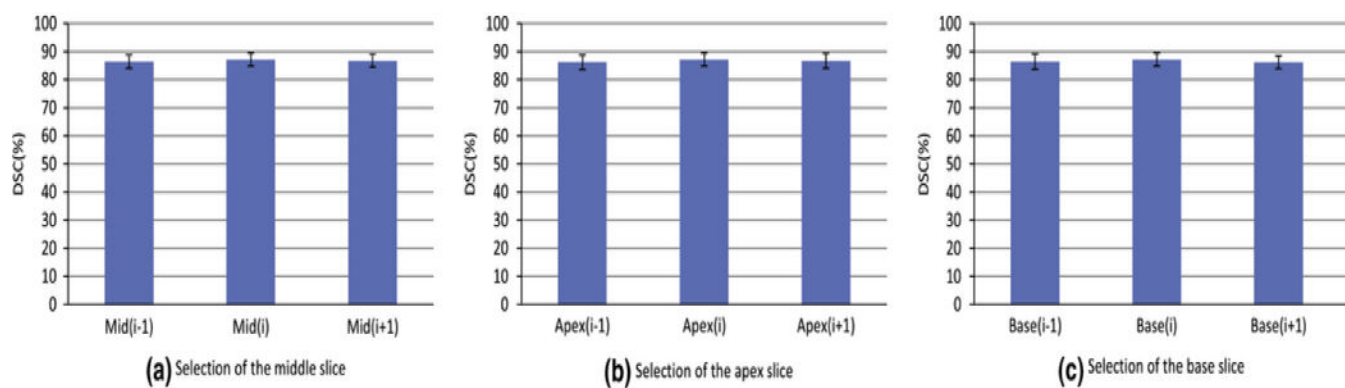


FIG. 9.
The influences of selecting three key slices on the final results.

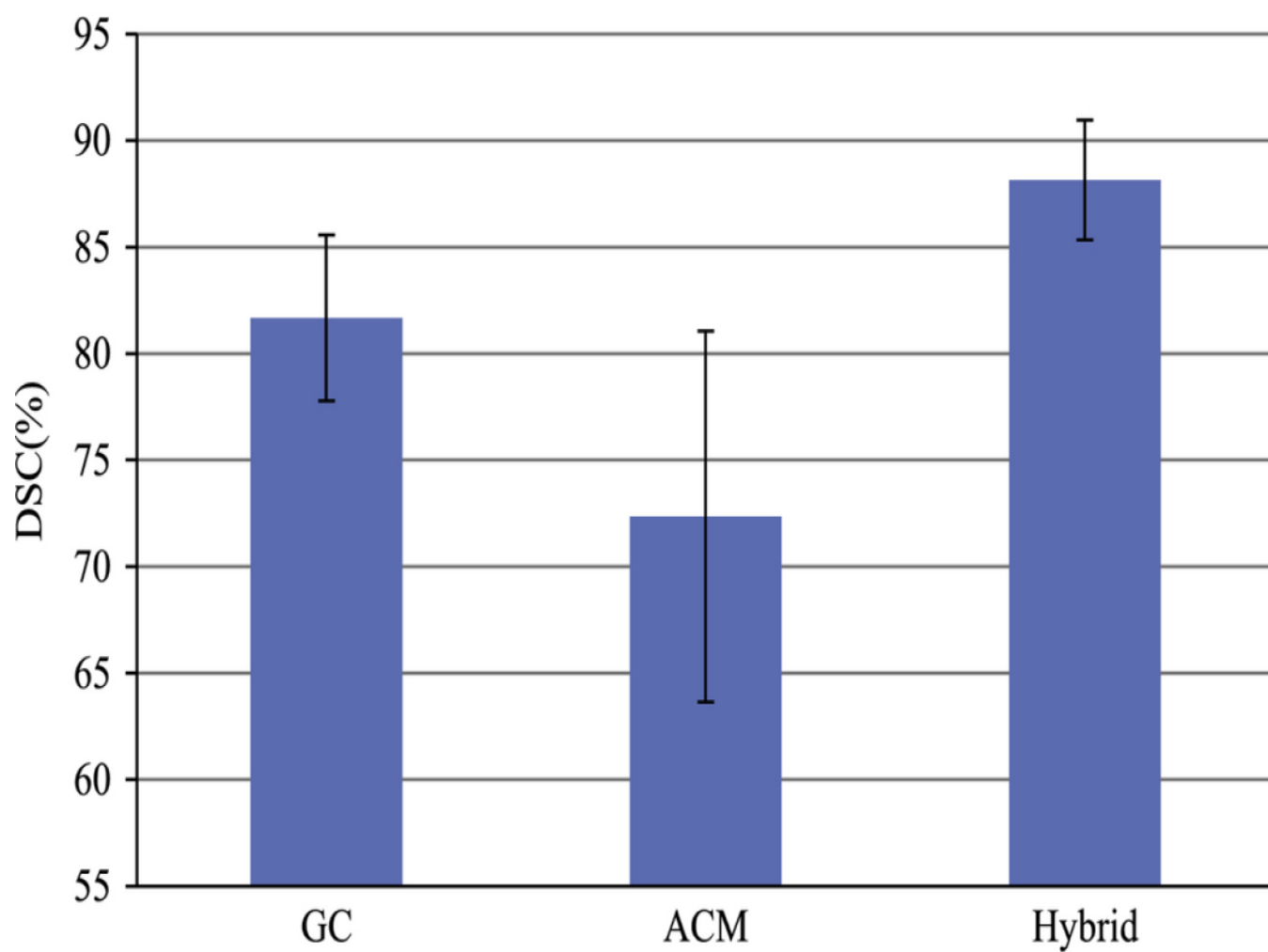


FIG. 10. Comparison of three segmentation methods: GC only, ACM only, and the proposed hybrid method.

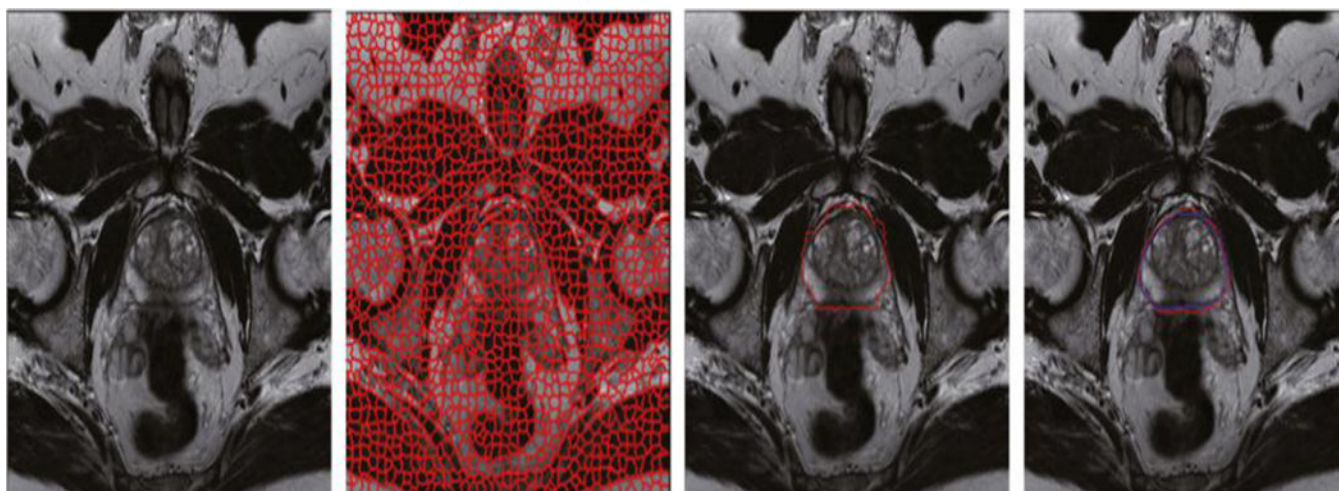


FIG. 11. The first image is one original slice of prostate MR. The second image is the corresponding supervoxel map. The third image is the segmentation result of GC. The fourth image is the final segmentation result improved by using AC. The blue color is the ground truth, while the red is the final segmentation result.

TABLE I

Quantitative results of the proposed method using our own data set. (DSC(%), RVD(%), HD(mm), and ASD(mm))

PT#	DSC	RVD	HD	ASD
Avg.	87.19	-4.58	9.92	2.07
Std.	2.34	7.59	1.84	0.35
Max	90.95	12.99	13.75	2.68
Min	82.77	-16.75	6.93	1.28

TABLE II

Quantitative results on PROMISE12 data set.

	DSC	RVD	HD	ASD
Avg.	88.15	2.82	5.81	2.72
Std.	2.80	9.56	2.01	0.77
Max	92.92	20.68	11.40	4.43
Min	81.80	-15.96	1.25	1.62

TABLE III

Comparison with 7 other prostate MR segmentation methods and with automatic version of our method using the PROMISE12 data set.

	Ours	grislies	ScrAutoPro	Imorphics	Robarts	ICProSeg	SBIA	V-net	Ours+Auto
DSC	88.2±2.8	86±6	90±1.1	88±3	85±5	84.6±4.3	85±4.4	87.1±4.2	87.8±2.9
HD	5.8±2.0	9.5±2.7	–	4.1±1.4	6.4±4.2	–	–	–	6.2±2.5

TABLE IV

Robustness of V-net method and our method: average of means \pm average of standard deviations of DSC across three different data sets.

	In-house	PROMISE12	ISBI
V-net	81.47 \pm 4.49	87.12 \pm 4.22	83.12 \pm 5.22
Ours	87.19 \pm 2.34	88.15 \pm 2.80	88.23 \pm 2.45